JMEPEG (2023) 16:1506–1517
https://doi.org/10.1007/s11665-023-08070-6

1059-9495/$19.00

TECHNICAL ARTICLE

Hydrothermal Synthesis of TiO_2@Sb-SnO_2 Nanocomposites Starting from Titanate Whiskers, $SnCl_4$, and $SbCl_3$ and their Electric Conductivity

Xiaonan Xie, Aili Wang, Hengbo Yin, Yun Ding, Mingxia Tian, Qinghua Xu, and Han Wang

Submitted: 12 December 2022 / Revised: 20 February 2023 / Accepted: 27 February 2023 / Published online: 13 March 2023

In our present work, we report the synthesis of Sb-doped SnO_2-coated TiO_2 (TiO_2@Sb-SnO_2) conductive nanocomposites by hydrothermal method. Firstly, titanate whiskers were hydrothermally synthesized at 175 °C using sodium hydroxide and metatitanic acid as starting materials with a molar ratio of 4:1. And then, the TiO_2@Sb-SnO_2 nanocomposites were hydrothermally synthesized with the use of the as-synthesized titanate whiskers, tin tetrachloride, and antimony trichloride as starting materials at 185 °C. In the hydrothermal reaction process, Sb-doped SnO_2 nanoparticles enhanced the phase transition from titanate to rutile TiO_2. The oxidation states of tin and antimony elements are Sn^{4+}, Sb^{5+}, and Sb^{3+}, respectively. TEM and HRTEM analyses indicated that the Sb-doped SnO_2 nanoparticles with an average particle size of around 1.5 nm were coated on the surfaces of TiO_2 nanoparticulates with an average particle size of around 20 nm. The TiO_2@(1%)Sb-(10%)SnO_2 nanocomposites had a minimum electric resistivity of 5.97×10^3 Ω·cm. Filling of the TiO_2@Sb-SnO_2 nanocomposites increased the electric conductivity of waterborne polyester films, endowing the polyester films with static electron dissipativity.

Keywords electric resistivity, polyester, rutile TiO_2, titanate whiskers, TiO_2@Sb-SnO_2 nanocomposites

1. Introduction

Nanocomposites with distinguished properties have been widely used as electrical conduction materials (Ref 1-3), sensors (Ref 4, 5), dielectric materials (Ref 6), additives in polymers (Ref 7), catalysts in thermal and photochemical reactions (Ref 8, 9), and pigments (Ref 10, 11). The synthesis and application of nanocomposites have attracted a great attention of researchers.

In the past decades, researchers found that low-cost *n*-type Sb-doped SnO_2 semiconductors exhibit high electrical conductivity, transparency, and band gap. The Sb-doped SnO_2 semiconductors can be used as functional materials in many fields, such as electrical conduction fillers for improving the conductivity of polycarbonate/acrylonitrile butadiene styrene (Ref 1), waterborne epoxy coating (Ref 2), rubber, and plastics (Ref 3); sensors for analyzing acetone, ethanol, liquefied petroleum gas (Ref 4), and formaldehyde (Ref 5); thermal insulation films for blocking ultraviolet light, reflecting near-infrared light, and maintaining visible light transparency (Ref 12-17); electrodes for degrading phenol, benzoic acid, norfloxacin, and tetracycline (Ref 18-21), inactivating *E.* coli (Ref 18), and oxidizing water (Ref 22). The Sb-doped SnO_2 semiconductors can also be used as laser stealth materials (Ref 23) and transparent electrodes for perovskite solar cell (Ref 24).

Sb-doped SnO_2 semiconductors could be synthesized by the chemical vapor deposition (Ref 25), aerosol-assisted chemical vapor deposition at 450 °C (Ref 26), oxygen-reactive DC and RF magnetron sputtering (Ref 27, 28), nonaqueous sol–gel (Ref 17, 29, 30), co-precipitation (Ref 16), and hydrothermal (Ref 31) methods using tin and antimony powders (Ref 25), butyl tin trichloride and antimony(III) ethoxide (Ref 26), Sn/Sb disk (Ref 27), Sb_2O_3 and SnO_2 (Ref 28), and $SnCl_4$ ($SnCl_2$) and $SbCl_5$ ($SbCl_3$, antimony(III) acetate, and antimony(III) ethoxide) (Ref 16, 17, 29, 31) as starting materials.

To obtain high electric conductivity, Sb-doped SnO_2 semiconductors are usually annealed at 450-550 °C (Ref 17, 26, 28-31). The electric resistivity of the annealed Sb-doped SnO_2 semiconductors ranges from 4.7×10^{-4} to 1.72×10^{-2} Ω·cm (Ref 17, 26-30). Without annealing at a high temperature, the electric resistivity of the as-synthesized (4-30 at.%) Sb-doped SnO_2 nanoparticles is at a relative low level, ranging from 1×10^4 to 1×10^6 Ω·cm (Ref 30).

To reduce the cost, Sb-doped SnO_2 semiconductors could be coated on oxides or mineral matrixes to form conductive composites. It was reported that the electric resistivity of porous coal slag@Sb-SnO_2 (Sb/Sn molar ratio of 1:6) powders prepared by calcination at 750 °C was 2.6×10^3 Ω·cm (Ref 32). The electric resistivity of TiO_2@(5%)Sb-SnO_2 nanocomposites prepared by calcination at 550 °C was 3.5×10^4 Ω·cm (Ref 3). The electric conductivity of rod-like TiO_2@Sb(10 at.%)-SnO_2 nanocomposites prepared at 75 °C was around 2×10^5 Ω·cm (Ref 33). The support type, Sb doping extent, and

Xiaonan Xie, Aili Wang, Hengbo Yin, Yun Ding, Mingxia Tian, Qinghua Xu, and **Han Wang**, Faculty of Chemistry and Chemical Engineering, Jiangsu University, Zhenjiang 212013, China. Contact e-mails: alwang@ujs.edu.cn and yin@ujs.edu.cn.

reaction temperature significantly affect the electric conductivity of supported Sb-SnO_2 nanocomposites. Although the supported Sb-doped SnO_2 nanocomposites had a larger electric resistivity than the "naked" Sb-doped SnO_2 semiconductors, the large-sized supported conductive nanocomposites not only decrease the cost but also facilely construct conductive networks in polymer matrixes, which effectively improves their electric conductivity.

In this work, we firstly synthesized sodium titanate whiskers by the hydrothermal method starting from metatitanic acid and sodium hydroxide. And then, the TiO_2@Sb-doped SnO_2 nanocomposites were hydrothermally synthesized using the as-synthesized titanate whiskers as TiO_2 precursors and $SnCl_4$/$SbCl_3$ as tin and antimony precursors. The as-synthesized TiO_2@Sb-doped SnO_2 nanocomposites exhibited good electric conductivity.

2. Experimental

2.1 Materials

Hydrated metatitanic acid ($H_2TiO_3 \cdot nH_2O$, 36.5 wt.% TiO_2) was purchased from the Jiangsu Taibai Group Co., Ltd. China. Sodium hydroxide, tin tetrachloride pentahydrate ($SnCl_4 \cdot 5H_2O$), antimony trichloride ($SbCl_3$), ammonia (28%), and hydrochloric acid (38%) were guaranteed reagents and purchased from the Chemical Reagent Co., Ltd. Shanghai, China.

2.2 Synthesis of Titanate Whiskers

Titanate whiskers were synthesized according to the procedures as follows. 43.5 g of hydrated metatitanic acid was dispersed in 100 mL of deionized water at room temperature (25 °C). After stirring for 30 min, the pH value of the aforementioned suspension was adjusted to *ca*. 2 by adding a sodium hydroxide (5 wt.%) aqueous solution. And then, a given amount of sodium hydroxide (20 wt.%) aqueous solution was added into the suspension under stirring at 300 rpm. The molar ratios of NaOH to metatitanic acid (H_2TiO_3) were set at 1:1, 4:1, and 6:1 by changing the amount of sodium hydroxide aqueous solution. After the reaction mixture was stirred at 300 rpm for 2 h, it was poured into Teflon-lined stainless-steel autoclaves and hydrothermally reacted in an electric oven at 175 °C for 24, 48, 72, and 96 h, respectively. When the reaction suspension was cooled to room temperature, the as-synthesized titanate whiskers were filtered, washed with deionized water to neutral, and dried at 110 °C for 12 h.

2.3 Synthesis of TiO_2@SnO_2 and TiO_2 @Sb-SnO_2 Nanocomposites

10 g of sodium titanate whiskers synthesized with an NaOH/H_2TiO_3 molar ratio of 4:1 at 175 °C for 96 h was dispersed in 50 mL of deionized water at 50 °C under stirring. Prescribed amounts of $SnCl_4 \cdot 5H_2O$ and $SbCl_3$ were dissolved in 50 mL of hydrochloric acid (2 $mol \cdot L^{-1}$) aqueous solution. The $SnCl_4$/$SbCl_3$ mixed aqueous solution was pumped into the sodium titanate whisker aqueous suspension with a peristaltic pump at a feeding rate of 1 $mL \cdot min^{-1}$ under stirring. At the same time, an ammonia aqueous solution (5 $mol \cdot L^{-1}$) was pumped into the aqueous suspension to control the pH value of reaction solution at *ca*. 7. After the $SnCl_4$/$SbCl_3$ mixed solution was added, the reaction solution was stirred at 50 °C for 2 h. The reaction solution was transferred into three Teflon-lined stainless-steel autoclaves each with a capacity of 100 mL. The hydrothermal reaction was conducted at 185 °C for 16 h in an electric oven. After the hydrothermal reaction, the as-synthesized TiO_2@S-nO_2 and TiO_2@Sb-SnO_2 nanocomposite samples were filtered and washed with deionized water until there were no Cl^- anions detected in filtrate by dropping several drops of $AgNO_3$ aqueous solution. And then, the washed samples were dried in an electric oven at 110 °C for 12 h.

The weight percentages of Sn in the TiO_2@SnO_2 nanocomposite samples were 5-20%. For the TiO_2@Sb-(10%)SnO_2 nanocomposite samples, the weight percentages of Sb were set at 1-5%. After the hydrothermal reaction, the contents of Sn and Sb in filtrates were at a negligible extent by ICP analysis, which indicates that Sb and Sn components were completely deposited in the as-synthesized TiO_2@SnO_2 and TiO_2@Sb-SnO_2 nanocomposites.

2.4 Preparation of TiO_2 @(1%)Sb-(10%)SnO_2 Nanocomposite-Filled Antistatic Polyester Films

TiO_2@(1%)Sb-(10%)SnO_2 nanocomposites were mixed with an environmentally friendly waterborne polyester paint. The contents of nanocomposites in the paint were set at 10-25 wt.%. The nanocomposite-filled polyester paint was coated on a smooth glass surface of 40×40 mm by a doctor blading coating method and dried naturally at room temperature for 24 h. The thicknesses of films were *ca*. 1 mm.

2.5 Characterization

The crystal structures of the titanate whisker, TiO_2@SnO_2, and TiO_2@Sb-SnO_2 samples were determined with the use of a powder XRD apparatus. The morphologies of the titanate whisker, TiO_2@SnO_2, and TiO_2@Sb-SnO_2 samples were observed on a scanning electron microscope. The microstructures of representative titanate whisker and TiO_2@Sb-SnO_2 samples were analyzed with the use of TEM and HRTEM techniques. The chemical states of tin and antimony components in representative TiO_2@SnO_2 and TiO_2@Sb-SnO_2 samples were analyzed with the use of XPS technique. The electric resistivity of the TiO_2@SnO_2, TiO_2@Sb-SnO_2, and TiO_2@Sb-SnO_2 nanocomposite-filled polyester films was measured on an ultra-high resistance microcurrent tester.

3. Results and Discussion

3.1 Evolution of Titanate Whiskers

Figure 1 shows the XRD patterns of the samples hydrothermally synthesized starting from sodium hydroxide and metatitanic acid with different NaOH/H_2TiO_3 molar ratios at 175 °C for prescribed time periods. When the molar ratio of NaOH to H_2TiO_3 was 1:1 and the hydrothermal reaction was conducted at 175 °C for 24-96 h, the XRD peaks of the as-synthesized samples were observed at (2θ) 25.3, 37.8, 48.1, 53.9, 55.1, 62.7, 68.8, 70.3, and 75.0°, respectively (Fig. 1a). These peaks belong to the characteristic ones of anatase TiO_2 (JCPDS No. 21–1272). The XRD peak intensity increased upon prolonging the hydrothermal reaction time, which reveals that the pro-

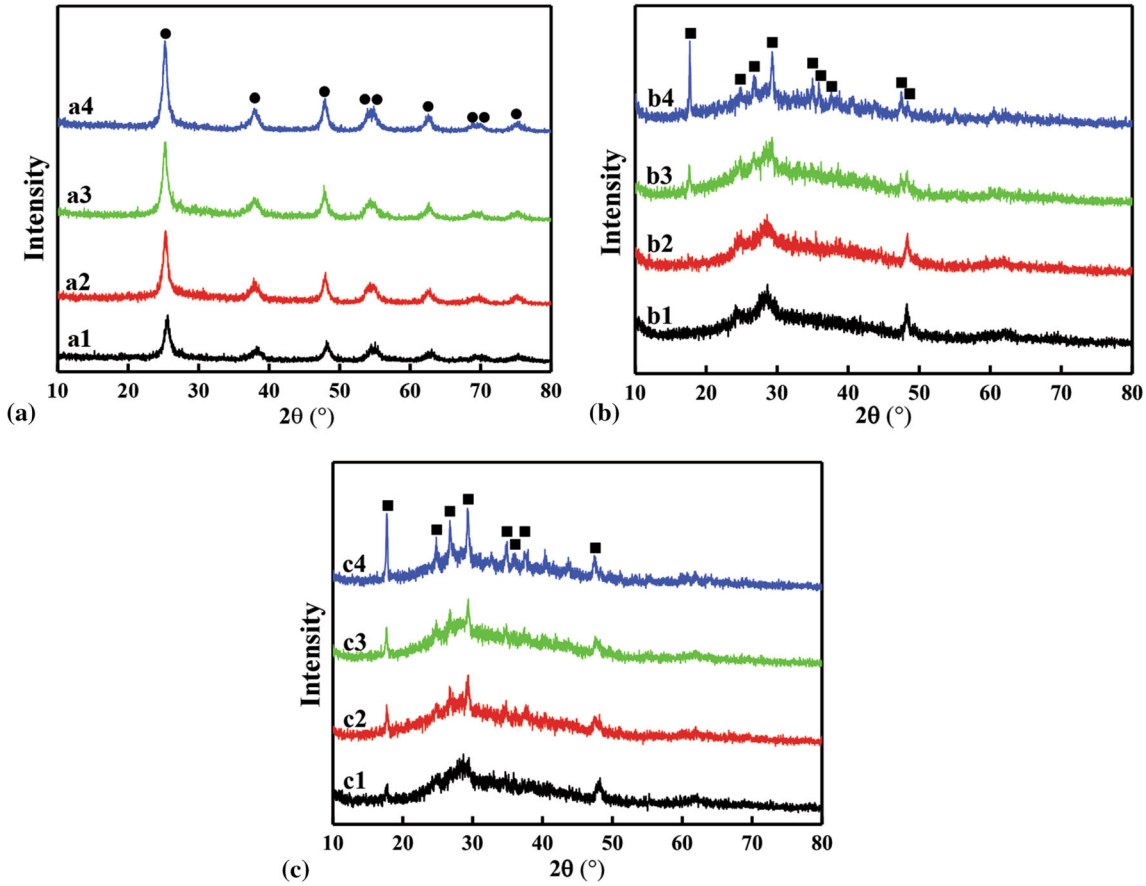

Fig. 1 XRD patterns of the samples hydrothermally synthesized with the $NaOH/H_2TiO_3$ molar ratios of (a1-a4) 1:1, (b1-b4) 4:1, and (c1-c3) 6:1 at 175 °C for given time periods of (a1,b1,c1) 24, (a2,b2,c2) 48, (a3,b3,c3) 72, and (a4,b4,c4) 96 h. (●) anatase TiO_2 (JCPDS No. 21–1272). (■) $Na_{0.98}H_{1.02}Ti_4O_9{\cdot}3.3H_2O$ (JCPDS No. 38–0221)

longing of hydrothermal reaction time increases the crystallinity of resultant anatase TiO_2 samples.

When the samples were hydrothermally synthesized with the $NaOH/H_2TiO_3$ molar ratio of 4:1 at 175 °C for 24-96 h, after washing and drying, several diffraction peaks were observed at (2θ) 17.6, 23.9, 26.5, 29.6, 35.3, 35.8, 37.6, 47.3, and 48.3° (Fig. 1b), which could be ascribed to those of distorted titanate salt, $Na_{0.98}H_{1.02}Ti_4O_9{\cdot}3.3H_2O$ (JCPDS No. 38–0221). The peak intensity increased with the prolonging of hydrothermal reaction time. While the hydrothermal reaction time was 72 h or longer, the appearance of a peak at (2θ) 17.6° indicates that the as-synthesized titanate salt has a layered structure.

As the molar ratio of NaOH to H_2TiO_3 was increased to 6:1, the XRD peaks of the distorted titanate salt ($Na_{0.98}H_{1.02}Ti_4O_9{\cdot}3.3H_2O$) were obviously observed for the washed and dried samples (Fig. 1c). The peak intensity of these samples was stronger than that of those samples synthesized with the $NaOH/H_2TiO_3$ molar ratio of 4:1. It is worthy to note that increasing the molar ratio of sodium hydroxide to metatitanic acid and prolonging the hydrothermal reaction time facilitate the formation of titanate salt.

We suggested that at a lower $NaOH/H_2TiO_3$ molar ratio of 1:1, metatitanic acid was converted to anatase TiO_2. Upon increasing the $NaOH/H_2TiO_3$ molar ratio to 4:1 or 6:1, sodium hydroxide could react with metatitanic acid to form layer-structured sodium tetratitanate and water molecules could intercalate into the layers of titanate salt. During washing process, Na^+ ions were substituted by H^+ ions, which results in the formation of $Na_{0.98}H_{1.02}Ti_4O_9{\cdot}3.3H_2O$. The evolution procedures are illustrated by the following equations.

$$H_2TiO_3 \xrightarrow[175^\circ C \text{ for } 24-96 \text{ h}]{NaOH/H_2TiO_3} \text{anatase } TiO_2 \quad \text{(Eq 1)}$$

$$H_2TiO_3 + NaOH + H_2O \xrightarrow[175^\circ C \text{ for } 24-96 \text{ h}]{NaOH/H_2TiO_3=4:1 \text{ and } 6:1} Na_2Ti_4O_9 \cdot nH_2O \quad \text{(Eq 2)}$$

$$Na_2Ti_4O_9 \cdot nH_2O \xrightarrow[\text{Drying at } 100^\circ C \text{ for } 12 \text{ h}]{\text{Washing with deionized water}} Na_{0.98}H_{1.02}Ti_4O_9 \cdot 3.3H_2O \quad \text{(Eq 3)}$$

The SEM images of the anatase TiO_2 samples show that these samples were composed of small-sized TiO_2 primary nanoparticles with the particle sizes of *ca*. 25 nm. The primary nanoparticles aggregated to form secondary particles with the sizes of *ca*. 1 μm (Fig. 2a1–a4).

When the titanate salt samples were synthesized with the $NaOH/H_2TiO_3$ molar ratio of 4:1, the washed and dried samples were composed of nanosized titanate whiskers (Fig. 2b1-b4). Diameters and lengths of the as-synthesized titanate whiskers increased with the prolonging of hydrothermal reaction time periods. When the titanate whiskers were

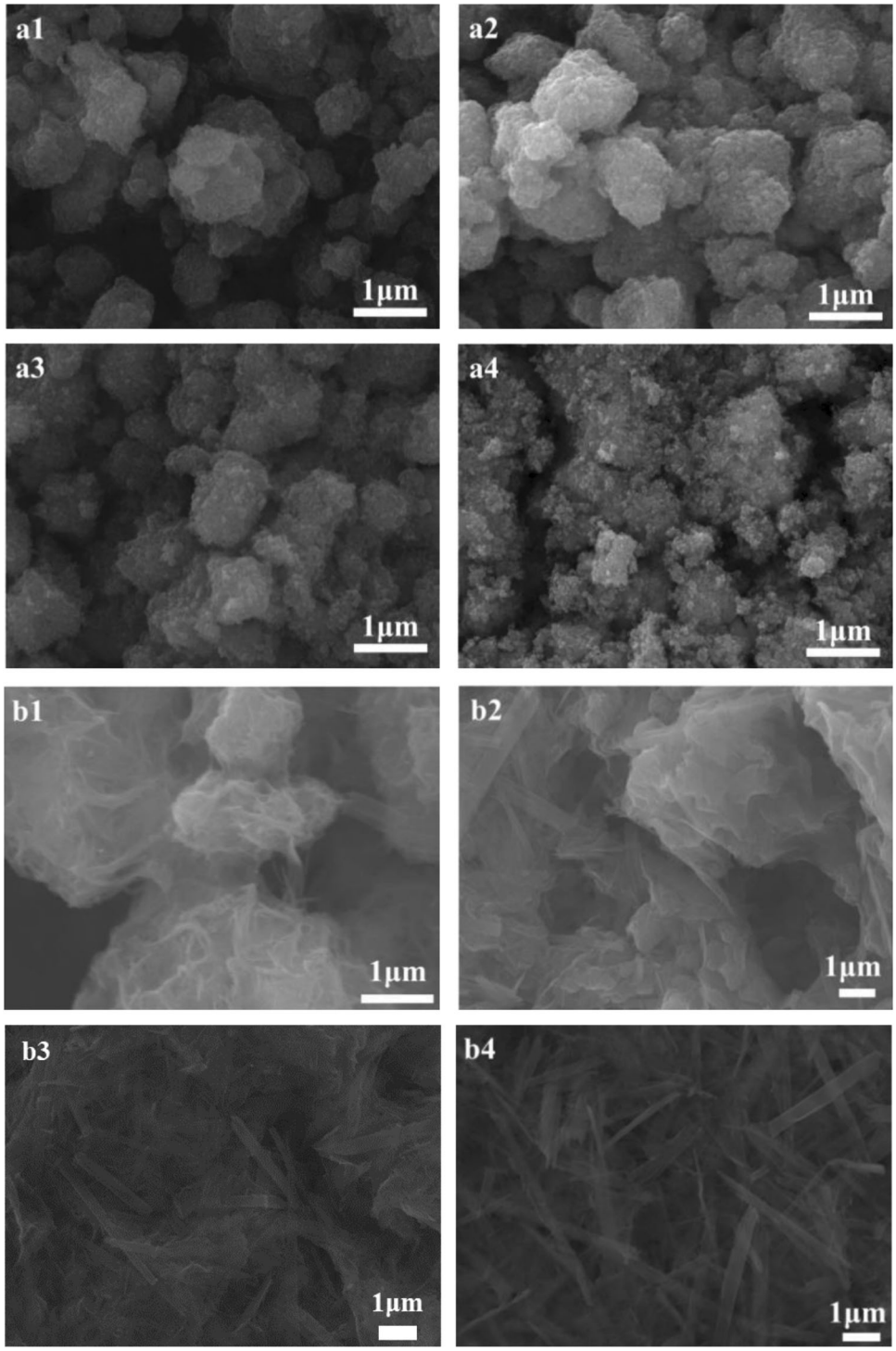

Fig. 2 SEM images of the samples hydrothermally synthesized with the $NaOH/H_2TiO_3$ molar ratios of (a1-a4) 1:1, (b1-b4) 4:1, and (c1-c3) 6:1 at 175 °C for given reaction time periods of (a1,b1,c1) 24, (a2,b2,c2) 48, (a3,b3,c3) 72, and (a4,b4,c4) 96 h. (d1) HRTEM image of the representative sample b4

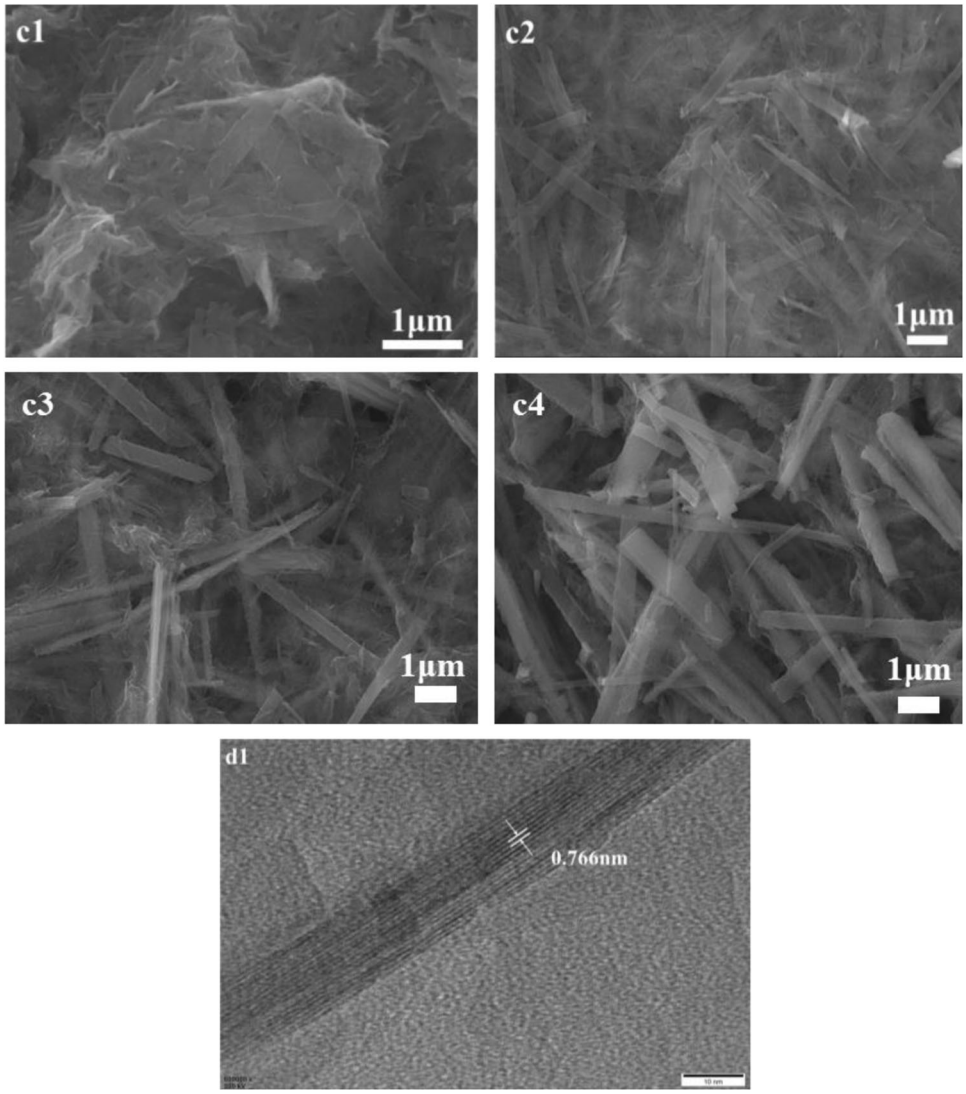

Fig. 2 continued

synthesized at 175 °C for 96 h, after washing and drying, their average diameter and length were 320 nm and 3.0 μm, respectively.

At the $NaOH/H_2TiO_3$ molar ratio of 6:1, diameters and lengths of the as-synthesized titanate whiskers also increased with the prolonging of hydrothermal reaction time periods (Fig. 2c1–c4). When the titanate whiskers were hydrothermally synthesized at 175 °C for 96 h, after washing and drying, their average diameter and length were 530 nm and 4.93 μm, respectively. Higher $NaOH/H_2TiO_3$ molar ratio and longer hydrothermal reaction time are beneficial to the crystal growth of titanate whiskers.

To determine the microstructures of titanate whiskers, a representative sample hydrothermally synthesized with the $NaOH/H_2TiO_3$ molar ratio of 4:1 at 175 °C for 96 h was analyzed by HRTEM. The HRTEM image shows that the as-synthesized titanate whiskers have a layered structure (Fig. 2d1). The layer distance is 0.766 nm, which is large enough for the intercalating of water molecules with a diameter of *ca*. 0.4 nm.

Considering that the titanate whisker sample synthesized with the $NaOH/H_2TiO_3$ molar ratio of 4:1 at 175 °C for 96 has a well crystal structure and small diameter, it was selected as the TiO_2 precursor for the synthesis of TiO_2@SnO_2 and TiO_2@Sb-SnO_2 conductive nanocomposites.

3.2 Evolution of TiO_2@SnO_2 and TiO_2@Sb-SnO_2 Nanocomposites

The titanate whiskers hydrothermally synthesized with the $NaOH/H_2TiO_3$ molar ratio of 4:1 at 175 °C for 96 h were used as TiO_2 precursors to synthesize TiO_2@SnO_2 and TiO_2@Sb-doped SnO_2 semiconductors. When the TiO_2@SnO_2 samples with 5-20% Sn were hydrothermally synthesized at 185 °C for 16 h, weak XRD peaks at 26.4 (shoulder), 34.1, and 51.9° ascribed to cassiterite SnO_2 phase (JCPDS No. 41–1445), peaks at 25.3, 37.8, 48.0, and 62.7° ascribed to anatase TiO_2 phase (JPCDS No. 21–1272), and strong peaks at 27.3, 35.9, 39.0, 41.1, 43.9, 54.1, 56.5, 62.7, 64.0, and 68.8° ascribed to rutile TiO_2 phase (JPCDS 21–1276) were observed (Fig. 3). The

XRD analysis revealed that during the hydrothermal reaction process, SnO_2 phase evolved. At the same time, titanate whiskers were converted to both anatase and rutile TiO_2. It is worthy to indicate that at a higher SnO_2 content, the peak intensity of rutile TiO_2 phase became stronger, whereas the peak intensity of anatase TiO_2 phase became weaker. It is reasonable to propose that SnO_2 crystallites could induce the phase transition from titanate to rutile even at a mild hydrothermal reaction temperature of 185 °C.

SEM images of the TiO_2@SnO_2 samples with 5-20% Sn contents show that these samples were composed of TiO_2 and SnO_2 nanoparticles (Fig. 4). The magnified SEM images show that the particle sizes of the samples ranged from 10 to 70 nm and their average particle sizes were *ca*. 30 nm. The elemental mapping images show that the tin and titanium elements uniformly dispersed in these samples, which indicates that the TiO_2 and SnO_2 nanoparticles well dispersed in the as-synthesized TiO_2@SnO_2 nanocomposites.

To increase the electric conductivity of TiO_2@SnO_2 nanocomposites, antimony component was added into the samples. The XRD patterns showed that at lower Sb contents of 1-2%, weak peaks at (2θ)25.2 and 37.8° ascribed to anatase TiO_2 phase (JPCDS No. 21–1272) and strong peaks at (2θ) 27.5, 35.9, 39.0, 41.1, 43.9,54.1, 56.6, 62.6, 63.9, and 69.0° ascribed to rutile TiO_2 phase (JPCDS No. 21–1276) were obviously observed (Fig. 5). The peak intensity of rutile TiO_2 phase was much stronger than that of anatase TiO_2 phase, indicating that rutile TiO_2 phase dominantly formed. Furthermore, a weak peak at (2θ) 52.4° ascribed to cassiterite SnO_2 (JPCDS No. 41–1445) was observed.

At larger Sb contents of 3-5%, rutile TiO_2 phase existed, whereas anatase TiO_2 phase disappeared. The addition of Sb component enhanced the phase transition from titanate to rutile TiO_2. A weak peak at (2θ) 52.4° ascribed to cassiterite SnO_2 phase was also observed. There were no antimony-containing compounds detected. It is worthy to note that with the addition of Sb component, the XRD peaks of cassiterite SnO_2 shift to large angles by 0.5° as compared to those of the TiO_2@SnO_2 samples. It could be explained as that antimony ions with smaller radius can substitute the Sn^{4+} ions of SnO_2 crystallites. With the increasing of substituting extent, the lattice constants of Sb-SnO_2 crystallites decrease, leading to the increase in diffraction angle (2θ) (Ref 14).

SEM images of the TiO_2@Sb-SnO_2 samples show that these samples were composed of TiO_2 and Sb-doped SnO_2 nanoparticles (Fig. 6). The magnified SEM images show that the particle sizes of the TiO_2@Sb-SnO_2 samples ranged from 10 to 70 nm and their average particle sizes were *ca*. 30 nm. The elemental mapping images show that the tin, antimony, and titanium elements uniformly dispersed in these samples, which indicates that the TiO_2 and Sb-SnO_2 nanoparticles could well disperse in the as-synthesized TiO_2@Sb-SnO_2 nanocomposites.

TEM and HRTEM images of the representative TiO_2@(1%,3%)Sb-(10%)SnO_2 samples are shown in Fig. 7. For the TiO_2@(1%)Sb-(10%)SnO_2 sample, the average particle size of Sb-SnO_2 nanoparticles was 1.5 nm. And the average particle size and particle size distribution of TiO_2 nanoparticulates were 19 and 12-70 nm, respectively. For the TiO_2@(3%)Sb-(10%) SnO_2 sample, the average particle size of Sb-SnO_2 nanoparticles was 1.6 nm. The average particle size and particle size distribution of TiO_2 nanoparticulates were 21 and 12-33 nm.

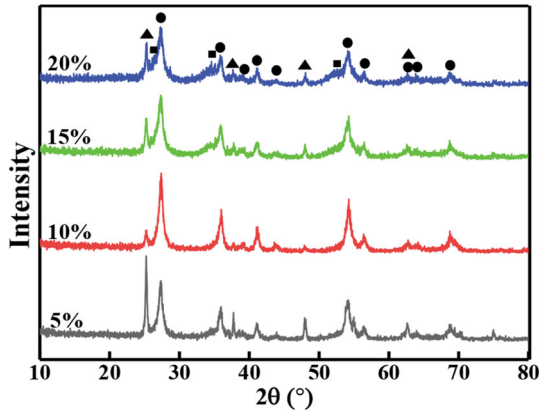

Fig. 3 XRD patterns of the TiO_2@SnO_2 samples with different Sn contents. (●) rutile TiO_2 (JCPDS No. 21–1276), (▲) anatase TiO_2 (JCPDS No. 21–1272), (■) cassiterite SnO_2 (JCPDS No. 45–1445)

The lattice fringes of TiO_2@(1%,3%)Sb-(10%)SnO_2 samples were 0.331 and 0.262 nm, which are ascribed to the lattice spacings of (1 1 0) and (1 0 1) planes of cassiterite SnO_2. And the lattice fringes of 0.328 nm are ascribed to the lattice spacing of (1 1 0) plane of rutile TiO_2.

The TEM and HRTEM analyses reveal that the small-sized Sb-doped SnO_2 nanoparticles well anchored at the surfaces of large-sized TiO_2 nanoparticulates. The TiO_2@Sb-SnO_2 samples had a core–shell structure.

The binding energies of Sn3d5/2 and Sn3d3/2 of the representative TiO_2@(10%)SnO_2, TiO_2@(1%)Sb-(10%)SnO_2, and TiO_2@(3%)Sb-(10%)SnO_2 were 486.4, 494.9; 486.6, 495; 486.6 and 495 eV, respectively (Fig. 8a). The distances between the Sn3d5/2 and Sn3d3/2 peaks were 8.5, 8.4, and 8.4 eV. The binding energy values and spin–orbit splitting of Sn3d5/2 and Sn3d3/2 indicate that the tin component in the samples is at Sn^{4+} oxidation state (Ref 5, 17, 32). However, the Sn3d5/2 and Sn3d3/2 peaks of the TiO_2@Sb-SnO_2 samples shifted to large values by 0.2 and 0.1 eV as compared to those of the TiO_2@SnO_2 sample. And the distances between the Sn3d5/2 and Sn3d3/2 peaks of the TiO_2@Sb-SnO_2 samples were slightly less than that of the TiO_2@SnO_2 sample. These changes could be ascribed to the substitution of Sn^{4+} ions in SnO_2 crystallites by antimony ions.

Considering the overlap of O1s and Sb3d5/2 peaks, the Sb3d3/2 peak was used to analyze the chemical state of antimony element in the nanocomposites. According to the reports, the binding energies of Sb3d3/2 peaks for Sb^{3+} and Sb^{5+} are 539.2-539.7 and 540.1-540.6 eV, respectively (Ref 3, 5, 32). To analyze the chemical state of antimony element, the binding energies of Sb3d3/2 peaks for Sb^{3+} and Sb^{5+} were set at 539.5 and 540.1 eV, respectively. The Sb3d3/2 peak was separated to two peaks by using an XPS peak split software. The peak splitting results show that the antimony element in TiO_2@(1%)Sb-(10%)SnO_2 and TiO_2@(3%)Sb-(10%)SnO_2 samples is at both Sb^{5+} and Sb^{3+} oxidation states (Fig. 8b and c). The ratios of Sb^{5+}/Sb^{3+} estimated according to their

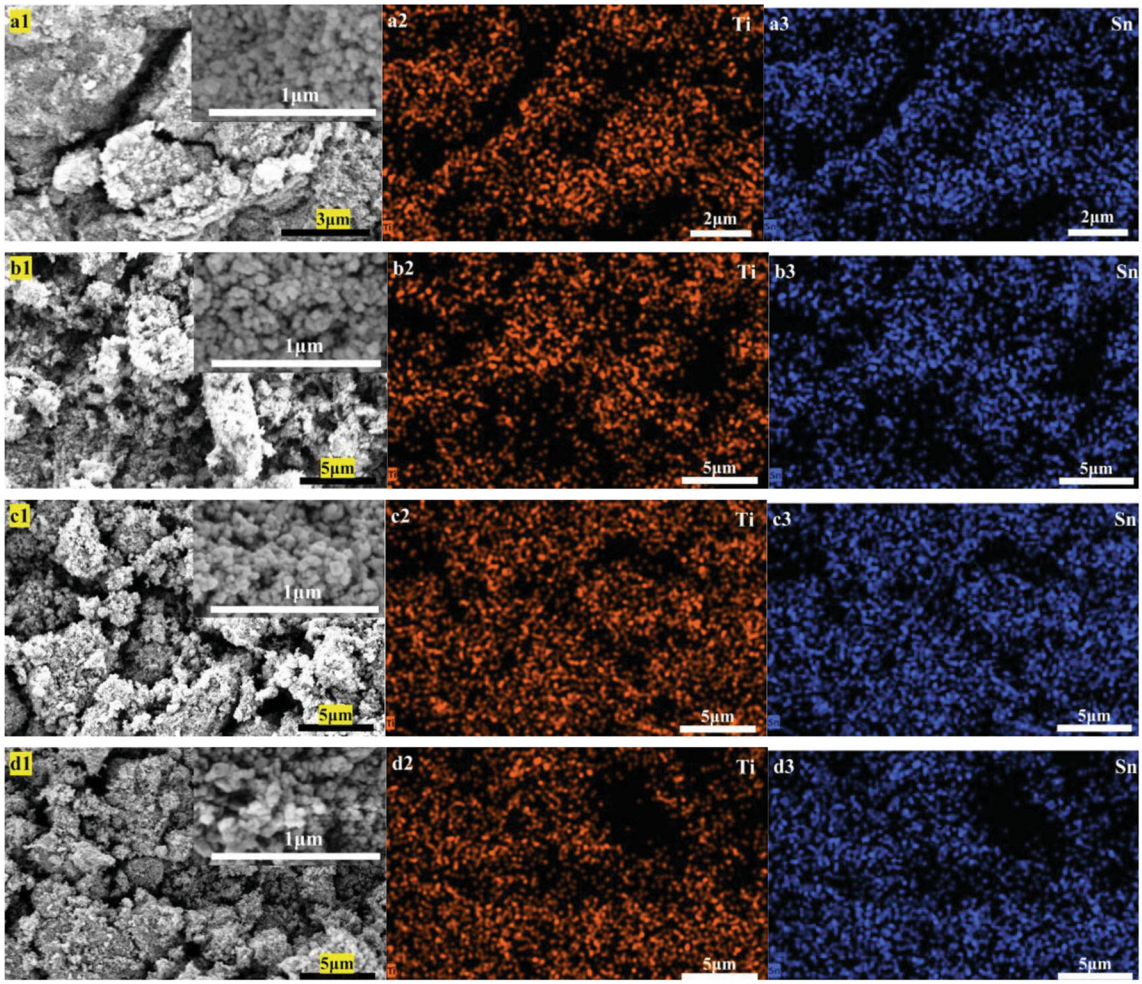

Fig. 4 SEM images and elemental mapping of the TiO_2@SnO_2 samples with different Sn contents. (a1-a3) 5% Sn, (b1-b3) 10% Sn, (c1-c3) 15% Sn, and (d1-d3) 20% Sn. The inserts in a1, b1, c1, and d1 are the magnified SEM images

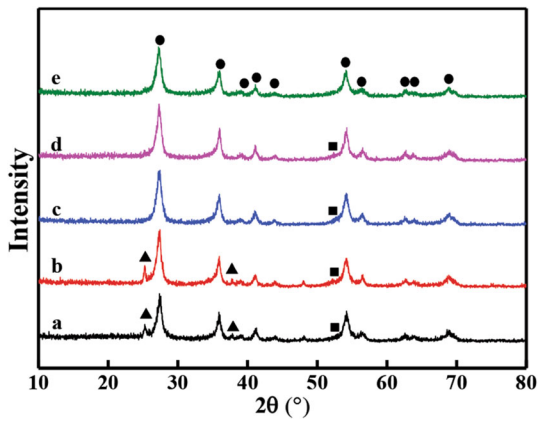

Fig. 5 XRD patterns of the TiO_2@Sb-SnO_2 samples with 10% Sn and different Sb contents of (a)1%, (b) 2% (c) 3%, (d) 4%, and (e) 5%. (●) rutile TiO_2 (JPCDS No. 21–1276), (▲) anatase TiO_2 (JPCDS No. 21–1272), (■) cassiterite SnO_2 (JPCDS No. 45–1445)

areas are 0.97:1 and 0.83:1, respectively. The XPS analysis reveals that during the hydrothermal synthesis process, part of Sb^{3+} was oxidized to Sb^{5+}.

3.3 Electric Conductivity of TiO_2@SnO_2 and TiO_2@Sb-SnO_2 Nanocomposites

Figure 9a shows the impacts of tin contents on the electric resistivity of TiO_2@SnO_2 nanocomposites. It was found that when the tin contents were increased from 5 to 10%, the electric resistivity of the TiO_2@SnO_2 nanocomposites dramatically decreased from 2.69×10^6 to 6.62×10^5 Ω·cm. Further increasing the tin content had no obvious effect on the electric resistivity. We suggest that at a tin content of 10%, the SnO_2 nanoparticles could be well coated at the surfaces of TiO_2 matrixes. Therefore, 10% tin content in the TiO_2/SnO_2 nanocomposite is enough to obtain a good electric conductivity.

When antimony dopant contents were 1-2%, the electric resistivity of the as-synthesized TiO_2@Sb-(10%)SnO_2 nanocomposites reached a lower level (Fig. 9b). At the antimony content of 1%, the minimum electric resistivity of 5.97×10^3 Ω·cm was obtained. Upon further increasing the antimony content, the electric resistivity slowly increased.

It has been suggested that when Sb^{5+} is the doping component in SnO_2 crystallite, Sb^{5+} introduces donor state (electron), which decreases the electric resistivity (Ref 3, 32). On the other hand, when Sb^{3+} and Sb^{5+} are the doping components in SnO_2 crystallite, Sb^{3+} introduces acceptor state (hole) and has a compensating effect on the donor state of Sb^{5+},

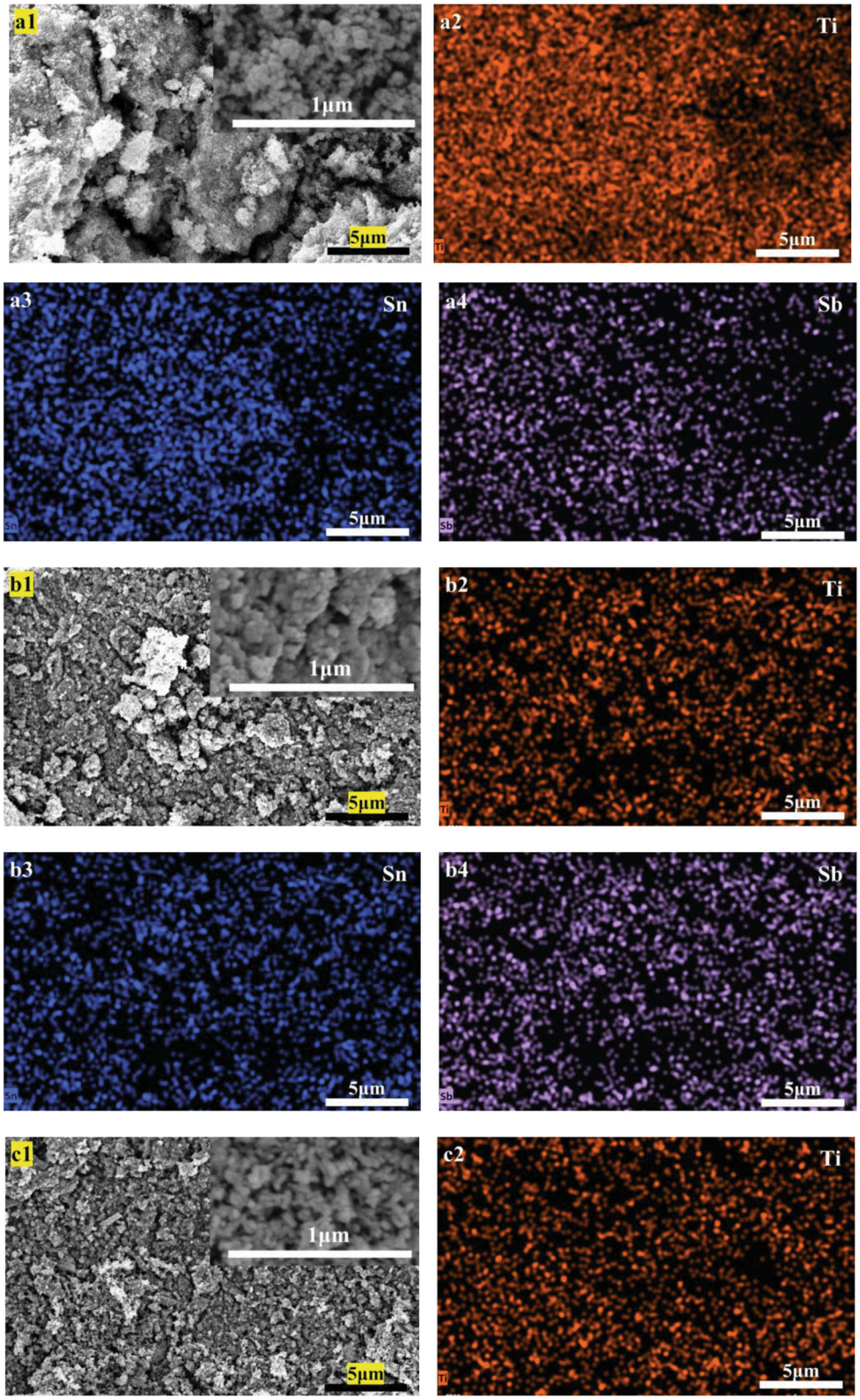

Fig. 6 SEM images and elemental mapping of the TiO_2@Sb-SnO_2 samples with 10% Sn and different Sb contents of (a1-a4)1%, (b1-b4) 2%, (c1-c4) 3%, (d1-d4) 4%, and (e1-e4) 5%. The inserts are the magnified SEM images

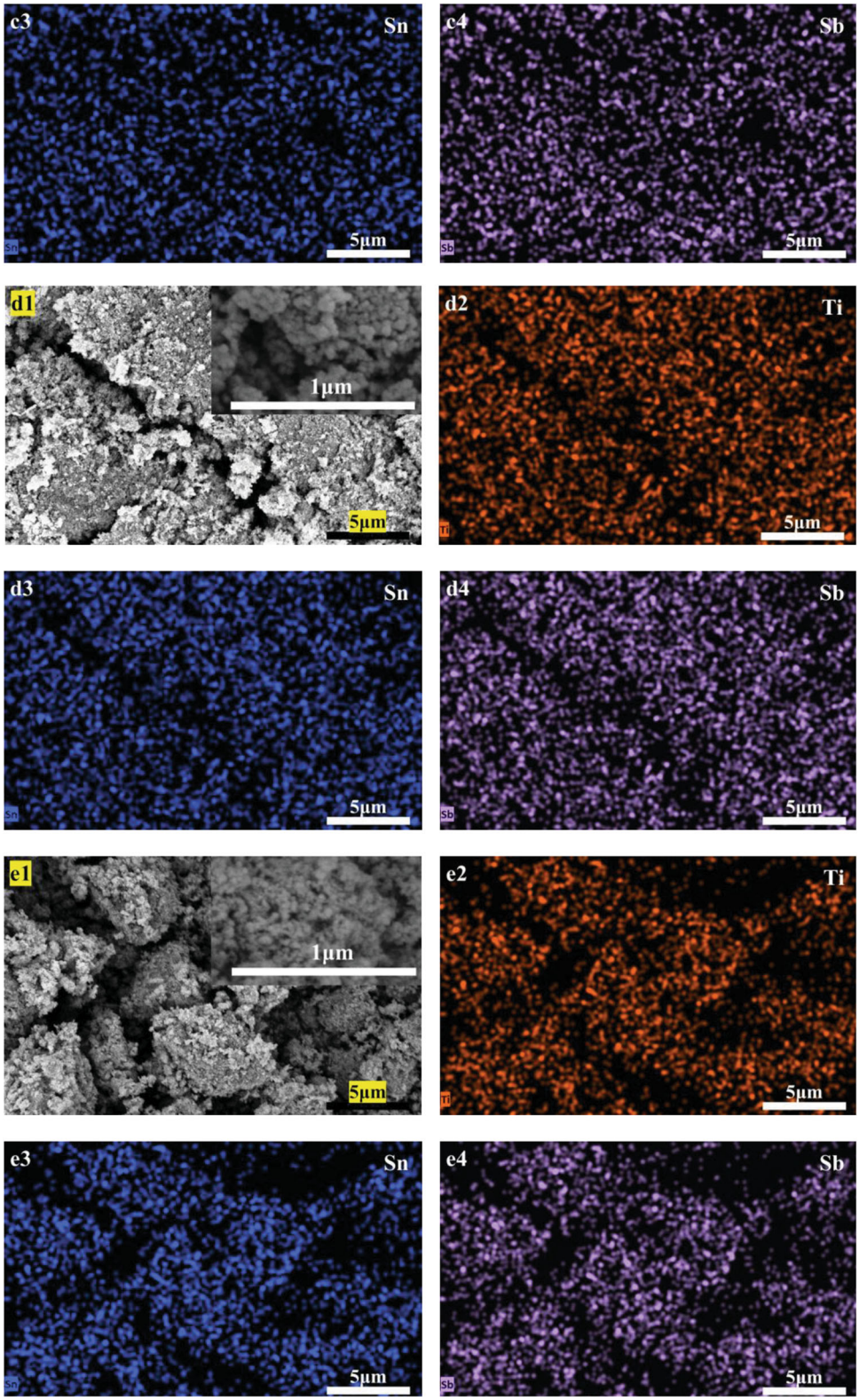

Fig. 6 continued

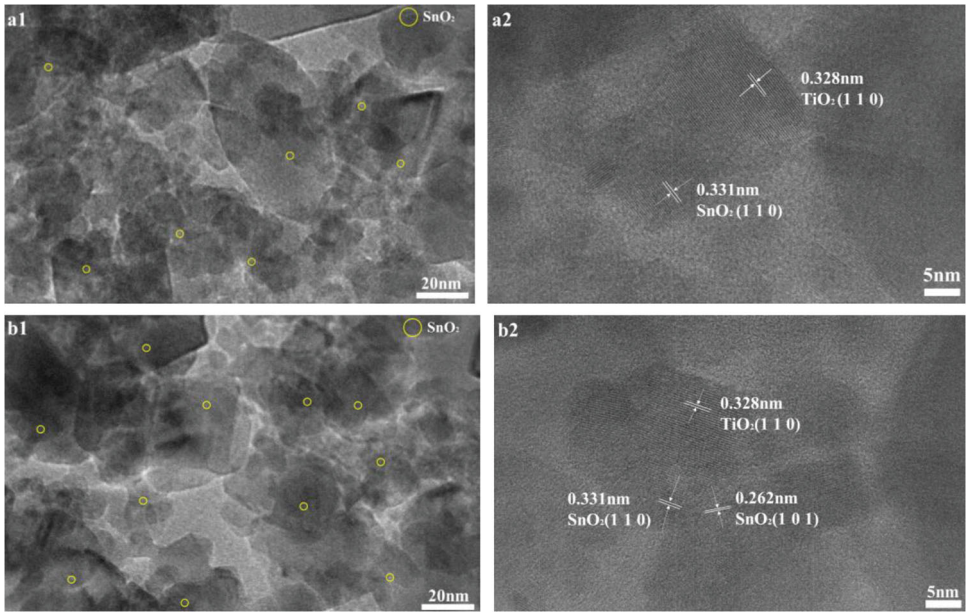

Fig. 7 TEM and HRTEM images of the representative (a1, a2) TiO_2@(1%)Sb-(10%)SnO_2 and (b1, b2) TiO_2@(3%)Sb-(10%)SnO_2 samples

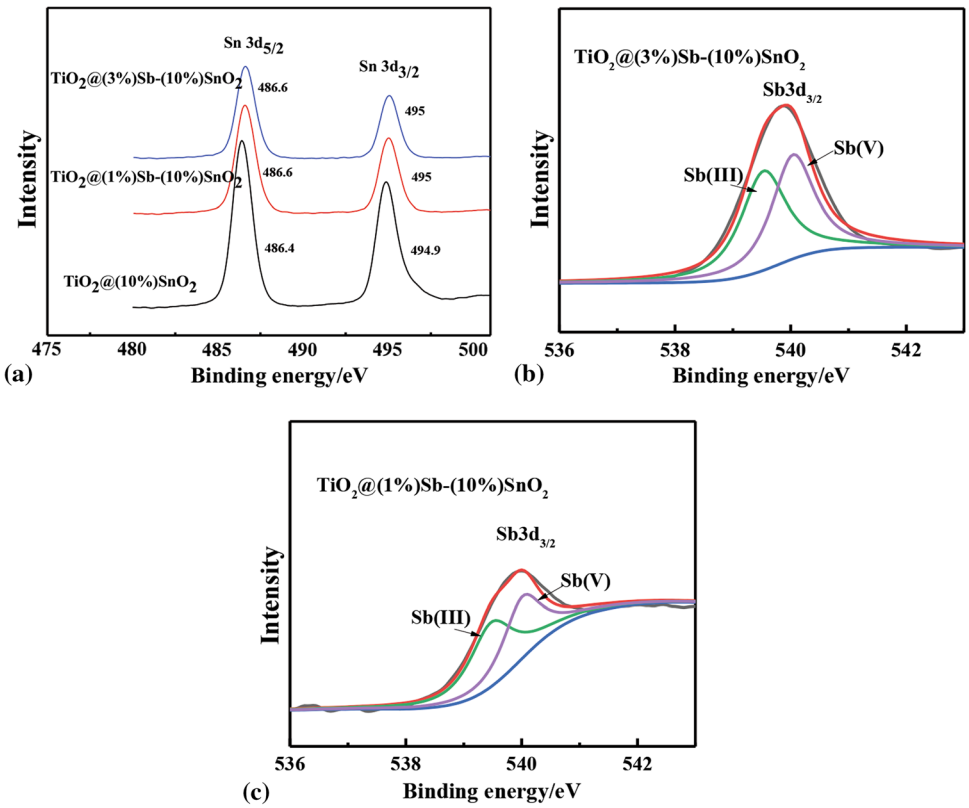

Fig. 8 XPS of the TiO_2@SnO_2 and TiO_2@(1%,3%)Sb-(10%)SnO_2 nanocomposites. (a) Sn3d and (b, c) Sb 3d3/2

which causes an increase in the electric resistivity of Sb-doped SnO_2 crystallite. Under our present hydrothermal reaction conditions, both Sb^{5+} and Sb^{3+} ions could substitute the Sn^{4+} ions in SnO_2 crystallites. A higher Sb^{5+}/Sb^{3+} ratio at a lower antimony content was favorable for obtaining higher electric conductivity. The antimony doping extent affected the Sb-SnO_2 crystal structure, which influences the electric conductivity.

3.4 Electric Conductivity of TiO_2@Sb-SnO_2 Nanocomposites-Filled Waterborne Polyester Paint Films

The electric resistivity of TiO_2@(1%)Sb-(10%)SnO_2 nanocomposite-filled waterborne polyester paint films decreased upon increasing the nanocomposite contents (Fig. 10).

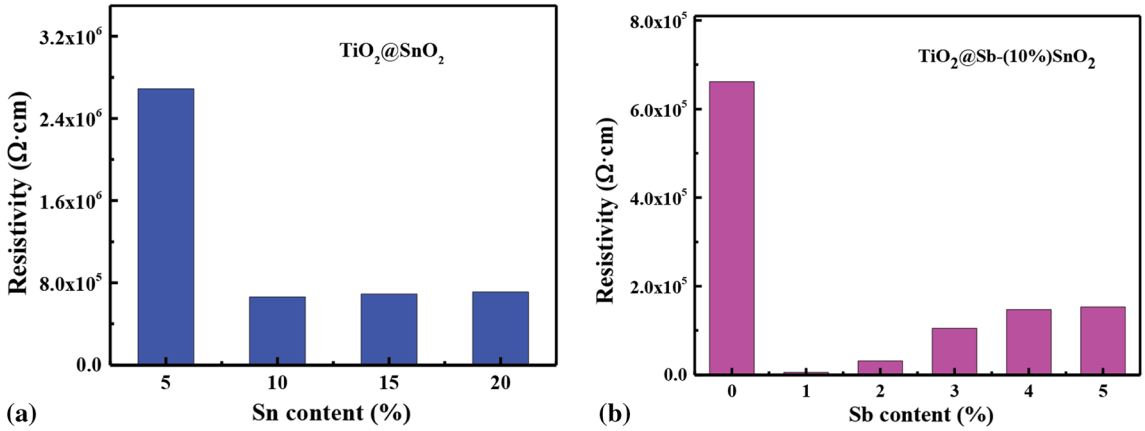

Fig. 9 Electric resistivity of the (a) TiO_2@SnO_2 and (b) TiO_2@Sb-(10%)SnO_2 nanocomposites

At a lower conductive nanocomposite content of 10 wt.%, the resistivity of the nanocomposite-filled polyester film was 6.59×10^{10} Ω·cm. The filling of conductive nanocomposite endowed the polyester paint film with static electron dissipativity. It is reasonably suggested that the as-synthesized TiO_2@(1%)Sb-(10%)SnO_2 nanocomposites could be used as effective conduction fillers to eliminate static electron accumulation in nonconductive polymers.

4. Conclusions

Titanate whiskers were hydrothermally synthesized at 175 °C using sodium hydroxide and metatatanic acid as starting materials with a molar ratio of 4:1 or 6:1. TiO_2@SnO_2 nanocomposites were hydrothermally synthesized at 185 °C with the use of the titanate whiskers and tin tetrachloride as titanium and tin precursors. The presence of SnO_2 phase promoted the phase transition from titanate to both anatase and rutile TiO_2. At 10 wt.% tin content, the electric resistivity of the as-synthesized TiO_2@(10%)SnO_2 nanocomposites was 6.62×10^5 Ω·cm.

When the titanate whiskers, tin tetrachloride, and antimony trichloride were used as titanium, tin, and antimony precursors, the rutile TiO_2@Sb-SnO_2 nanocomposites were hydrothermally synthesized at 185 °C. The Sb-doped SnO_2 nanoparticles could enhance the phase transition from titanate to rutile TiO_2 when the Sb content was above 2 wt.%. The TiO_2@(1%)Sb-(10%)SnO_2 nanocomposites had a minimum electric resistivity of 5.97×10^3 Ω·cm.

In the TiO_2@SnO_2 and TiO_2@Sb-SnO_2 nanocomposites, the oxidation state of tin component is Sn^{4+}. And the oxidation states of antimony component are both Sb^{5+} and Sb^{3+}. TEM and HRTEM analyses show that the Sb-doped SnO_2 nanoparticles with an average particle size of *ca*. 1.5 nm were coated on the surfaces of rutile TiO_2 nanoparticulates with an average particle size of *ca*. 20 nm.

The filling of the as-synthesized TiO_2@Sb-SnO_2 nanocomposites promoted the electric conductivity of waterborne polyester paint films, which endows the polyester films with static electron dissipativity.

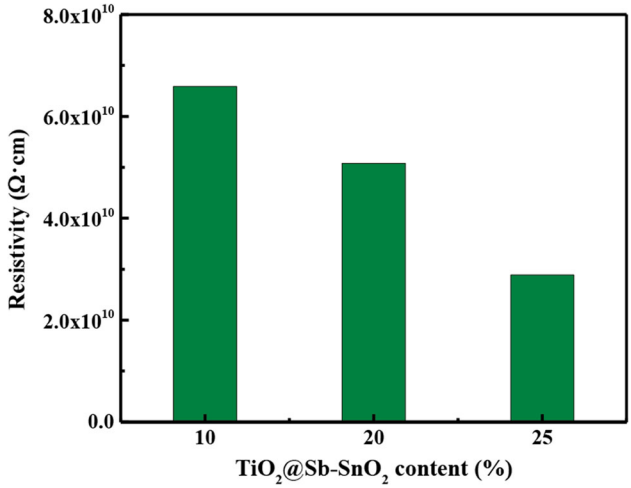

Fig. 10 Electric resistivity of the TiO_2@(1%)Sb-(10%)SnO_2 nanocomposite-filled waterborne polyester films

Acknowledgments

Our present work was financially supported by the fund from the Liaoning Science and Technology Department, China (2021JH1/10400063).

References

1. T. Chen, P. Xue, and M. Jia, The Property of Polycarbonate/Acrylonitrile Butadiene Styrene-Based Conductive Composites Filled by Nickel-Coated Carbon Fiber and Nickel-Graphite Powder, *Polym. Composite*, 2017, **38**, p 157–163.
2. T. Wang, H. Ge, and K. Zhang, A Novel Core-Shell Silica@Graphene Straticulate Structured Antistatic Anticorrosion Composite Coating, *J. Alloys Compd.*, 2018, **745**, p 705–715.

3. X. Li, J. Qian, J. Xu, Y. Sun, and L. Liu, Synthesis and Electrical Properties of Antimony-Doped Tin Oxide-Coated TiO_2 by Polymeric Precursor Method, *Mat. Sci. Semicon. Proc.*, 2019, **98**, p 70–76.
4. A.R. Babar, S.S. Shinde, A.V. Moholkar, C.H. Bhosale, J.H. Kim, and K.Y. Rajpure, Sensing Properties of Sprayed Antimony Doped Tin Oxide Thin Films: Solution Molarity, *J. Alloys Compd.*, 2011, **509**, p 3108–3115.
5. Y.D. Wang, I. Djerdj, M. Antonietti, and B. Smarsly, Polymer-Assisted Generation of Antimony-Doped SnO_2 Nanoparticles with High Crystallinity for Application in Gas Sensors, *Small*, 2008, **4**, p 1656–1660.
6. J. Guo, Z. Chen, Z.M. El-Bahy, H. Liu, H.M. Abo-Dief, W. Abdul, K. M. Abualnaja, A.K. Alanazi, P. Zhang, M. Huang, G. Hu, and J. Zhu, Tunable Negative Dielectric Properties of Magnetic $CoFe_2O_4$/Graphite-Polypyrrole Metacomposites, *Adv. Compos. Hybrid Mater.*, 2022, **5**, p 899–906.
7. T. Liu, Z. Li, T. Jiang, S. Xi, Y. Li, J. Guo, M. Huang, H. Algadi, X. Ye, and Q. Jiang, Improvement of Thermodynamic Properties of Poly (Butanediol Sebacate-Butanediol Terephthalate) (PBSeT) Composites Based on the Dispersion of $PCaCO_3$@Tannic Acid Formed by Complexation of Tannic Acid and Ti, *Adv. Compos. Hybrid Mater.*, 2022, **5**, p 2787–2800.
8. A. Wang, D. Yu, H. Yin, and W. Yuan, Preparation of Bimetallic Cu_xAg_y Nanoparticles and their Catalytic Performance in Hydrogenation of 4-Nitrophenol with H_2 to 4-Aminophenol, *Catal. Lett.*, 2022, **152**, p 3691–3703.
9. M. Eqi, C. Shi, J. Xie, F. Kang, H. Qi, X. Tan, Z. Huang, J. Liu, and J. Guo, Synergetic Effect of Ni-Au Bimetal Nanoparticles on Urchin-Like TiO_2 for Hydrogen and Arabinose Co-Production by Glucose Photoreforming, *Compos. Hybrid Mater.*, 2023, **6**, p 5.
10. W. Cao, A. Wang, and H. Yin, Preparation of TiO_2@ZrO_2@SiO_2@-MAA Nanocomposites and Impact of Layer Structure on Pigmentary Performance, *Mater. Chem. Phys.*, 2021, **263**, p 124403.
11. L. Shen, W. Cao, A. Wang, and Hengbo Yin, Preparation of TiO_2@ZrO_2@AlOOH@Polymethyl Acrylic Acid Nanocomposites and the Impact of Layer Structure on Color Scheme, Photocatalytic Activity, and Dispersion Stability, *Ind. Eng. Chem. Res.*, 2020, **59**, p 21811–21821.
12. D. Fang, H. Yu, M. Dirican, Y. Tian, J. Xie, D. Jia, C. Yan, Y. Liu, C. Li, H. Liu, J. Wang, F. Tan, G. Chen, X. Zhang, and J. Tao, Disintegrable, Transparent and Mechanically Robust High-Performance Antimony Tin Oxide/Nanocellulose/Polyvinyl Alcohol Thermal Insulation Films, *Carbohyd. Polym.*, 2021, **266**, p 118175.
13. J. Qu, J. Song, J. Qin, Z. Song, W. Zhang, Y. Shi, T. Zhang, H. Zhang, R. Zhang, Z. He, and X. Xue, Transparent Thermal Insulation Coatings for Energy Efficient Glass Windows and Curtain Walls, *Energ. Build.*, 2014, **77**, p 1–10.
14. M. Wang, Y. Xu, Y. Liu, W. Wu, and S. Xu, Synthesis of Sb-Doped SnO_2 (ATO) Hollow Microspheres and Its Application in Photo-Thermal Shielding Coating, *Prog. Org. Coat.*, 2019, **136**, p 105229.
15. H. Li, L. Song, H. Liu, J. Li, A. Yang, C. Sun, R. Li, Y. Fu, and C. Yu, Antimony-Doped Tin Oxide Embedding Graphene-Based Aerogel for Infrared Barriering, *Ceram. Int.*, 2019, **45**, p 7894–7905.
16. B. Shen, Y. Wang, L. Lu, and H. Yang, pH-Dependent Doping Level and Optical Performance of Antimony-Doped Tin Oxide Nanocrystals as Nanofillers of Spectrally Selective Coating for Energy-Efficient Windows, *Ceram. Int.*, 2021, **47**, p 20335–20340.
17. J. Mazloom, F.E. Ghodsi, and M. Gholami, Fiber-Like Stripe ATO (SnO_2:Sb) Nanostructured Thin Films Grown by Sol-Gel Method: Optical, Topographical and Electrical Properties, *J. Alloys Compound*, 2013, **579**, p 384–393.
18. S.Y. Yang, D. Kim, and H. Park, Shift of the Reactive Species in the Sb −SnO_2-Electrocatalyzed Inactivation of E. Coli and Degradation of Phenol: Effects of Nickel Doping and Electrolytes, *Environ. Sci. Technol.*, 2014, **48**, p 2877–2884.
19. X. Cui, G. Zhao, Y. Lei, H. Li, P. Li, and M. Liu, Novel Vertically Aligned TiO_2 Nanotubes Embedded with Sb-Doped SnO_2 Electrode with High Oxygen Evolution Potential and Long Service Time, *Mater. Chem. Phys.*, 2009, **113**, p 314–321.
20. S. Man, H. Bao, K. Xu, H. Yang, Q. Sun, L. Xu, W. Yang, Z. Mo, and X. Li, Preparation and Characterization of Nd-Sb co-Doped SnO_2 Nanoflower Electrode by Hydrothermal Method for the Degradation of Norfloxacin, *Chem. Eng. J.*, 2021, **417**, p 129266.
21. Z. Liu, M. Zhu, L. Zhao, C. Deng, J. Ma, Z. Wang, H. Liu, and H. Wang, Aqueous Tetracycline Degradation by Coal-Based Carbon Electrocatalytic Filtration Membrane: Effect of Nano Antimony-Doped Tin Dioxide Coating, *Chem. Eng. J.*, 2017, **314**, p 59–68.
22. Y. Sun, W.D. Chemelewski, S.P. Berglund, C. Li, H. He, G. Shi, and C. B. Mullins, Antimony-Doped Tin Oxide Nanorods as a Transparent Conducting Electrode for Enhancing Photoelectrochemical Oxidation of Water by Hematite, *ACS Appl. Mater. Interfaces*, 2014, **6**, p 5494–5499.
23. Y. Zhang, Q. Shao, B. Zhao, B. Zhang, V. Murugadoss, S. Wu, T. Ding, and Z. Guo, Facile Bioactive Yeast Cell Templated Synthesis of Laser Stealth Antimony Doped Tin Oxide Hollow Microspheres, *Colloid Surface A*, 2019, **583**, p 123965.
24. Y. Bai, Y. Fang, Y. Deng, Q. Wang, J. Zhao, X. Zheng, Y. Zhang, and J. Huang, Low Temperature Solution-Processed Sb:SnO_2 Nanocrystals for Efficient Planar Perovskite Solar Cells, *Chemsuschem*, 2016, **9**, p 2686–2691.
25. I.M. Costa, Y.N. Colmenares, P.S. Pizani, E.R. Leite, and A.J. Chiquito, Sb Doping of VLS Synthesized SnO_2 Nanowires Probed by Raman and XPS Spectroscopy, *Chem. Phys. Lett.*, 2018, **695**, p 125–130.
26. S.D. Ponja, B.A.D. Williamson, S. Sathasivam, D.O. Scanlon, I.P. Parkin, and C.J. Carmalt, Enhanced Electrical Properties of Antimony Doped Tin Oxide Thin Films Deposited via Aerosol Assisted Chemical Vapour Deposition, *J. Mater. Chem. C*, 2018, **6**, p 7257–7266.
27. J. Montero, J. Herrero, and C. Guillén, Preparation of Reactively Sputtered Sb-Doped SnO_2 Thin Films: Structural, Electrical and Optical Properties, *Sol. Energ. Mat. Sol. C.*, 2010, **94**, p 612–616.
28. J. Ni, X. Zhao, X. Zheng, J. Zhao, and B. Liu, Electrical, Structural, Photoluminescence and Optical Properties of p-Type Conducting, Antimony-Doped SnO_2 Thin Films, *Acta Mater.*, 2009, **57**, p 278–285.
29. S.S. Lekshmy, G.P. Daniel, and K. Joy, Microstructure and Physical Properties of Sol Gel Derived SnO_2: Sb Thin Films for Optoelectronic Applications, *Appl. Surf. Sci.*, 2013, **274**, p 95–100.
30. V. Müller, M. Rasp, G. Štefanić, J. Ba, S. Günther, J. Rathousky, M. Niederberger, and D. Fattakhova-Rohlfing, Highly Conducting Nanosized Monodispersed Antimony-Doped Tin Oxide Particles Synthesized via Nonaqueous Sol-Gel Procedure, *Chem. Mater.*, 2009, **21**, p 5229–5236.
31. M. Zhang, Y. Wang, Y. Ma, X. Wang, B. Zhao, and W. Ruan, Study of Charge Transfer Effect in Surface-Enhanced Raman Scattering (SERS) by Using Antimony-Doped Tin Oxide (ATO) Nanoparticles as Substrates with Tunable Optical Band Gaps and Free Charge Carrier Densities, *Spectrochim. Acta A*, 2022, **264**, p 120288.
32. J. Zhang, J. Zuo, Y. Jiang, A. Ju, D. Zhu, J. Zhang, and C. Wei, Synthesis and Characterization of Composite Conductive Powders Prepared by Sb-SnO_2-Coated Coal Gasification Fine Slag Porous Microbeads, *Powder Technol.*, 2021, **385**, p 409–417.
33. Z. Chen, M. Gu, F. Wang, C. Gao, P. Liu, Y. Ding, S. Zhang, and M. Yang, Conductive TiO_2 Nanorods via Surface Coating by Antimony Doped Tin Dioxide, *Mater. Chem. Phys.*, 2019, **225**, p 181–186.